Computational Fluid Dynamics of a Corrugated Plate-and-Frame Heat Exchanger Used for Ocean Thermal-Energy Conversion

Albert S. Kim, Ph.D.[1]; Hyeon-Ju Kim, Ph.D.[2]; Ho-Saeng Lee, Ph.D.[3]; and Myung-Jin Koh[4]

Abstract: Computational fluid dynamics (CFD) simulations were employed in this paper to analyze the dynamic flow patterns within extremely thin slit spaces of two corrugated heat exchanger (HEx) plates. The entire plates are 1.0 m long and wide and 6.5 mm high, and the top and bottom parts consist of six unit plates of the same size (1.0 m long and 16.7 cm wide). A digital geometry of the assembled HEx was prepared as a stereolithography (STL) file (exported from AutoCAD), having excessive geometrical complexity. In this work, a numerical algorithm to reconstruct the STL file is developed, which converts a complex STL file consisting of skew triangles to one having a simple grid structure and an even size-distribution of surface triangles. The whole STL file is split into 36 square pieces (SPs), and each SP is meshed individually using NETGEN, and these meshes are merged as one for OpenFOAM-based CFD simulations. Finally, the flow and pressure profiles are obtained in the low Reynolds number region. The current CFD method with the *split-and-merge* scheme will be continuously used for the design and optimization for ocean thermal energy conversion technology in the future. **DOI: 10.1061/(ASCE)EE.1943-7870.0001688.** © *2020 American Society of Civil Engineers.*

Introduction

In the 21st century, the depletion rates of conventional energy sources increase dramatically. To overcome the energy-scarce situation, it is emphasized that renewable energy technologies should reach a near-commercial stage within a few decades (Abas et al. 2015). The availability of conventional energy will rapidly decrease during the 2030s–2040s, even with a reasonable estimation of the energy demand (i.e., approximately 1% per year) (Ul'yanin et al. 2018). For the daily life of human beings in the current century, electricity and fresh water are two vital resources, for both of which steady production exists as a critical issue within engineering practices. Renewable energy is naturally replenishing and inexhaustible in principle within duration, but is limited by transfer rates of mass and momentum in the available amount per unit of time, having types of biomass, hydropower, geothermal, wind, and solar energies (US EIA 2018).

In addition to the established major types of renewable energy, several ocean-based engineering methods regarding renewable energy production exist, which include wave (Younesian and Alam 2017), tide (Brown et al. 2017), and thermal energy. Specifically, ocean thermal energy conversion (OTEC) has a long history following Jules Verne's classic science-fiction, adventure novel *20,000 Leagues Under the Sea* followed by the pioneering efforts by Dr. Jacques-Arsene d'Arsonval and his student Georges Claudes (D'Arsonal 1881), who was an inventor of the open-cycle OTEC (OC-OTEC). After Claudes' death, an American electrical engineer, in addition to being one of the foremost Nicolai Tesla historians, Leland Anderson, revised Claudes OC-OTEC and applied for a US patent on a Sea Water Power Plant, later called a closed-cycle (CC) OTEC. In the CC-OTEC process, a working fluid (instead of sea water) is used for efficient heat transfer (Mac Takahashi 2000; Wang et al. 2010). In Hawai'i, two major long-term experiments were conducted as historical landmarks within OTEC history. In 1979, an offshore CC-OTEC barge plant, called the Mini-OTEC, was built and successfully operated from August to November of that year using ammonia as a working fluid. An overview and discussion regarding the commercialization potential of CC-OTEC can be found elsewhere (Vega 2010; Vega and Michaelis 2010; Vega 2012). Due to the enormous amount of ocean thermal energy, OTEC has been closely considered within the engineering field as a potential future fuel production technology (Syamsuddin et al. 2015; Banerjee et al. 2017; Rani et al. 2017). As OTEC technology can be classified into open-, closed-, and hybrid-cycles, CC-OTEC is preferred to others due to its better performance; although, OC-OTEC causes much fewer environmental concerns. General OTEC practices are primarily limited by fundamental demands of a large-size evaporator and steady pumping of cold deep seawater (DSW). The OTEC performance and DSW intake are limited due to the low-temperature gradient between the warm surface and cold deepsea waters and the installation/maintenance costs of long high-pressure pipes, respectively.

[1]Professor, Dept. of Civil and Environmental Engineering, Univ. of Hawai'i at Mānoa, 2540 Dole St., Holmes Hall 383, Honolulu, HI 96822 (corresponding author). ORCID: https://orcid.org/0000-0002-9027-4616. Email: albertsk@hawaii.edu

[2]Principal Researcher, Offshore Plant and Marine Energy Research Division, Korea Research Institute of Ships and Ocean Engineering, 32 Yuseong-Daero, 1312 Beon-Gil, Daejeon 305-343, Republic of Korea. Email: hyeonju@kriso.re.kr

[3]Principal Researcher, Seawater Energy Plant Research Center, Korea Research Institute of Ships and Ocean Engineering, 124-32 Simchungsu-Gil, Jukwang-Myon, Kosung-Gun, Gangwon-do 24747, Republic of Korea. Email: hslee@kriso.re.kr

[4]Ph.D. Student, Dept. of Civil and Environmental Engineering, Univ. of Hawai'i at Mānoa, 2540 Dole St., Holmes Hall 383, Honolulu, HI 96822. Email: myungj@hawaii.edu

Note. This manuscript was submitted on April 28, 2019; approved on October 14, 2019; published online on April 6, 2020. Discussion period open until September 6, 2020; separate discussions must be submitted for individual papers. This paper is part of the ***Journal of Environmental Engineering***, © ASCE, ISSN 0733-9372.

Background of OTEC

Typical temperature ranges of the surface seawater (SSW) and DSW are 25°C–28°C and 5°C–8°C, respectively. The cooling source of the condenser is the cold DSW, taken from 0.5 to 1.5 km below the sea water surface.

The cyclic steps of OC-OTEC are as follows. The warm seawater enters the evaporator maintained under pressure below the vapor pressure of the inlet seawater stream. The entered SSW evaporates, and the vapor migrates to the turbine installed between the evaporator and condenser. The turbine rotates and generates electricity as the vapor flow passes through it. The thermally exhausted vapor condenses on the surfaces of the heat exchanger (HEx). The condensed water is freshwater, having the same quality to that of the distilled water. The DSW temperature increases from approximately 5°C to 7°C–8°C while being pumped from the deep sea to the condenser above sea level. Discharged DSW has a higher temperature due to the exchanged latent heat for the phase conversion from the vapor gas to liquid water. As the OTEC performance is sensitive to both SSW and DSW temperatures, HEx should be well maintained to produce high efficiency for the steady production of electricity and fresh water.

The Rankine cycle is used for CC-OTEC, characterized using the isenthalpic ensemble (constant enthalpy), having the number of molecules N, pressure P, and enthalpy H as controlling variables. CC-OTEC also has similar cyclic steps to those of OC-OTEC. In the CC-OTEC process, a working fluid (often organic) is used for efficient heat transfer, and the steps are as follows. A cooled-down working fluid (from the previous cycle) of high pressure enters the HEx. Heat is externally applied to the working fluid at a constant pressure, and once the temperature reaches the boiling point, the liquid phase is converted to a gas phase. During this step, the temperature remains constant, and entropy and enthalpy increase. A dry, saturated vapor expands through a turbine and rotate the turbine to generates electric power. During this thermal work done by the evaporated gas flow, the temperature decreases with a little increase in entropy. Finally, wet vapor leaves the turbine and condenses in a condenser, and afterwards, the cycle returns to the first step. The temperature remains the same as the condensation temperature while entropy significantly decreases due to the gas-to-liquid phase change. In the CC-OTEC using a working fluid (such as R32) (Yoon et al. 2015), heat transfer into and out of the working fluid within the HEx significantly influences the hydraulic residence time and, hence, overall OTEC performance. In a practical design analysis, the HEx's were often treated as one-dimensional units, characterized simply by a few material and operational parameters. In the computational fluid dynamics (CFD) literature, full-scale simulations inside a HEx of a high aspect ratio (i.e., a corrugated plate HEx) were not actively investigated due to the geometrical complexity and computational cost.

High concentrations of inorganic solutes and less-identified species (from SSW) may cause internal fouling phenomena of the HEx, primarily due to the chemical adsorption. Because the entering streams exist as natural seawater (without any treatment) from the surface and floor of the ocean, this adsorption is often irreversible and, hence, makes a chemical cleaning process less efficient. The physical cleaning of the adsorptive fouling requires disassembling of the HExs, often at a high cost, especially for corrugated plate HExs. One possible physical cleaning method involves injecting cleaning balls, which will collide with the fouled internal surfaces a number of times to provide linear and angular impacts on the fouled surfaces. The motion of the injected balls is governed by the gravitational/buoyant forces, hydrodynamic forces in the complex flow field, and linear/angular impacts generated during particle collisions with internal wall surfaces of the HExs. Due to the opaque property of the HEx materials, it is difficult to observe, experimentally, the cleaning ball dynamics within the narrow spaces of the large fluid volume. As natural seawater from two sources are used for heating and cooling sources without pretreatment, maintaining the HEx in a minimum adsorption rate is one of the critical factors for successful operations.

The overarching goal of the current project is to fully optimize the performance of a HEx in a sequence by analyzing the fluid dynamic patterns, understanding specific heat-exchanging phenomena, and finding optimal conditions for the in-situ cleaning methods. A corrugated HEx of specific interior geometry was selected and purchased by project collaborators, and a large stereolithography (STL) file of the complex HEx geometry was provided for simulation research. Facets of the STL file have a very skewed structure, so that in this work, we focus on geometrical reconstruction, parallel mesh generation, and flow-pattern simulations for efficient CFD simulations.

Simulation Methods

Mesh Generation

Splitting Stereolithography

The geometrical specification of the HEx consisting of six unit rectangular plates is listed in Table 1. The total length and width of the assembled HEx is 1,012 and 939.38 mm, respectively. The distance between the lowest and the highest points is 6.5 mm. However, these two points may not be on the same position on the respective plane but off from the same vertical line because the top and bottom surfaces are corrugated. The internal volume was calculated as 3.253 L using an open-sourced software admesh (Martin 1998). The volume-equivalent height is calculated as 3.43 mm, which is the total volume divided by the projected surface area (i.e., a product of the length and the width). The aspect ratios of length and width to the equivalent height are 292.40 and 274.67, respectively. These extremely high aspect ratios (close to 300) made the NETGEN meshing process exceptionally long and challenging because tetrahedron meshing starts from the side boundaries and conforms the mesh near a central zone of the object.

Fig. 1 shows the geometry of the HEx plate, an STL file exported from AutoCAD software, and provided for us by the main project team. In general, using an STL file for CFD work has some advantages. The STL format is of industry standard, and both ASCII and binary data types are acceptable within standard engineering software programs. The file structure is straightforward,

Table 1. Specifications of the assembled HEx, consisting of six rectangular unit-plates, where H_{eq} is the volume-equivalent height

Variable	Value	Unit
Internal volume	3.25349	L
Length, L	1,012.0	mm
Width, W	936.00	mm
Height, H	6.00	mm
Height, H_{eq}	3.42	mm
Aspect ratio	$L/H_{eq} = 292.40$	—
	$W/H_{eq} = 274.67$	—
Highest point	(1,355.0, 282.5, 13.28746)	mm
Lowest point	(343.0, 129.5, 6.78746)	mm
Max height	6.50	mm

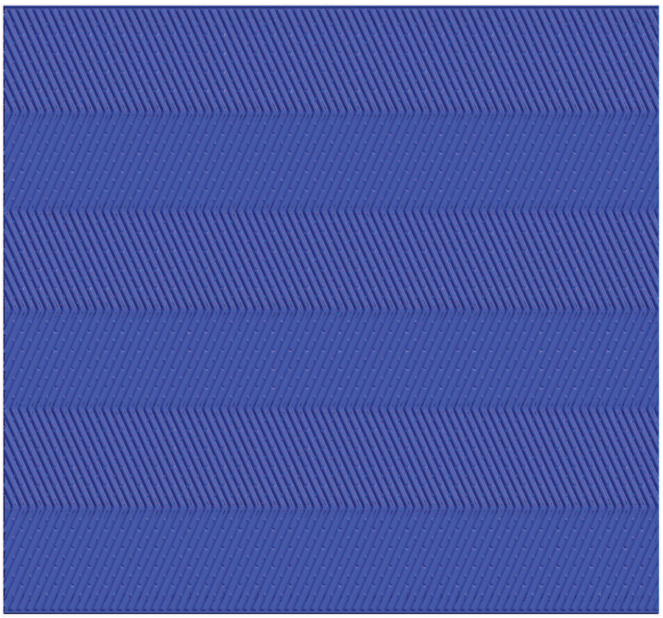

Fig. 1. (Color) STL view of the full HEx, having 4,515,782 facets.

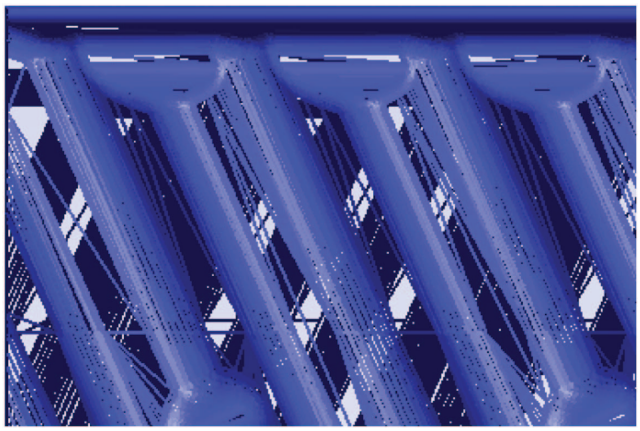

Fig. 2. (Color) Detailed view of local surface structure, consisting of highly skewed triangles.

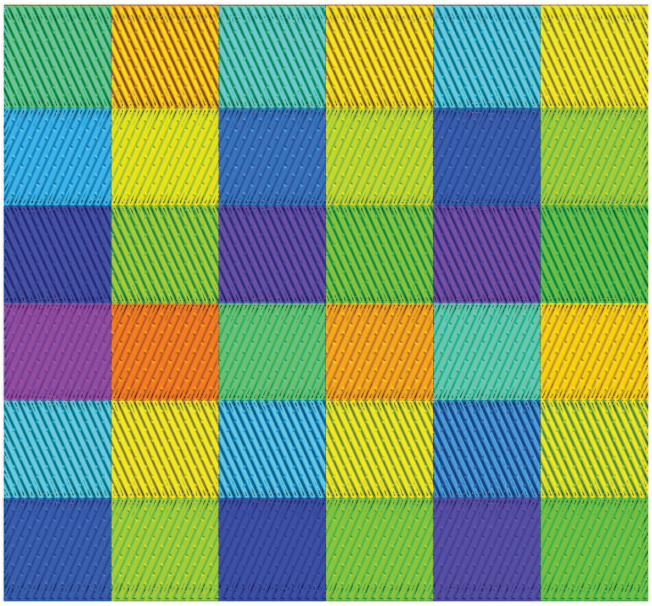

Fig. 3. (Color) Visualization of 36 split pieces of the HEx STL structure using gmsh. The combined structure is identical to that of Fig. 1.

which stores the geometrical information of only surface elements of outer boundaries. A unit surface element consists of a triangle represented using three position vectors of vertices and a normal vector of the element, called a facet. In practices, an STL file is inputted within a mesh generation software, such as gmsh (Geuzaine and Remacle 2009; Marchandise et al. 2012), NETGEN (Yilmaz and Ozturan 2015), and tetgen (Si 2013, 2015), which generate tetrahedral meshes of various formats. The choice of software depends on the meshing speed and, more importantly, its adaptability to CFD solvers with numerical stability and convergence during the solving process. First, we loaded the entire HEx-STL file to NETGEN to generate the mesh. However, this initial meshing trial was not successful, perhaps due to the large size and complicated local geometries stored in the HEx-STL file.

STL Local Complexity

The local triangular shapes of the STL file were visually investigated, as shown in Fig. 2, in which the lines indicate edges of triangles forming the surface topography of the HEx surfaces. As shown, there are a number of highly skewed facets having one of three angles close to 0 radian. If the facet is almost equilateral, having each of the three angles at approximately $\pi/3$, then the skewness approaches 0. If one of the angles is close to 2π and so the other two angles are almost zero, then the skewness is close to 1, which is, in general, not acceptable for proper mesh generation. Tetrahedron-based meshes are less preferred because facet edges are not consistently aligned in the flow direction as compared to to the hexahedral meshes. In addition, highly skewed facets often make the tetrahedron-based meshing more difficult.

STL Splitting

The possible method to generate the HEx mesh within a reasonable time is to split it into small pieces and reconstruct STL facets to have similar-sized triangles. The perfect uniqueness of facets may also cause a technical problem in that the facets should be small enough, but this problem can be resolved in the meshing process. This reconstruction must be as computationally intensive as the original meshing work unless the HEx dimension is effectively reduced. As the entire HEx consists of six long rectangular plates, as shown in Fig. 3, each of the long plates was subdivided into six square pieces (SPs) of equal size. The whole HEx is split into 36 equal-sized SPs using the software Netfabb version 2018.0 (industrial-strength 3D printing software for Windows from Auto-Desk version 2016) and are visualized using gmsh (Geuzaine and Remacle 2009; Marchandise et al. 2012) in Fig. 3. Each HEx piece is 167 mm long and 156 mm wide, which gave us much more flexibility to create the entire HEx mesh.

Stereolithographic Reconstruction

Meshing each of the 36 split-STL files was also not successful due to the the geometrical complexity of the facets, intrinsically remained in the STL files. An additional reason can be attributed to the irregular distribution of triangular sizes in addition to the high level of skewness. To reconstruct the SPs with even distribution of facet sizes, the ray-tracing algorithm (Levoy 1990; Nah et al. 2014; Fang et al. 2015; Wald et al. 2017) was employed, modified, and applied in this study. A sample result of the STL reconstruction is shown in Fig. 4(a), of which surface covers a wider region (i.e., the left top corner of the whole plate shown in Fig. 3) to that used for

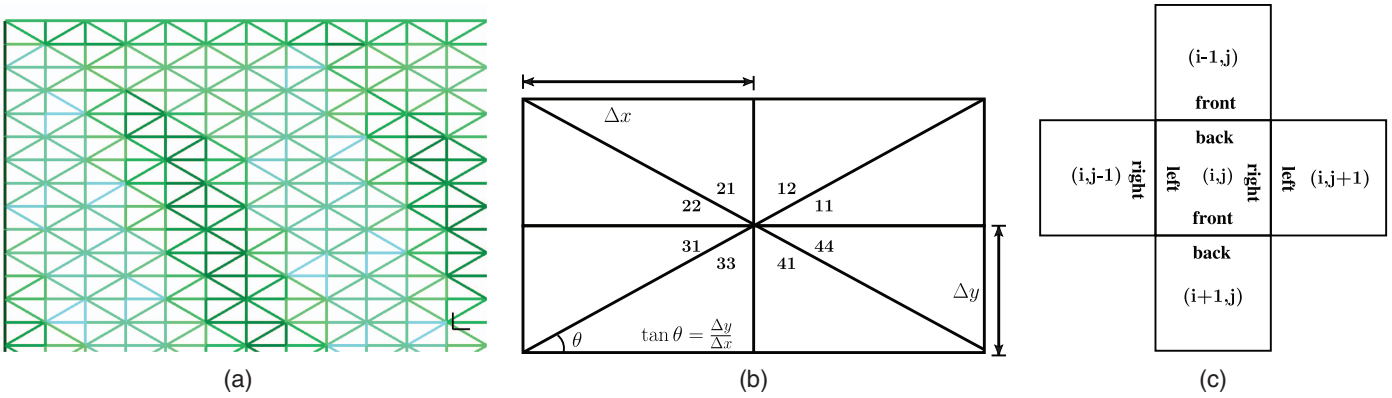

Fig. 4. (Color) Partial view of (a) reconstructed STL file, consisting of (b) a set of four equal-sized unit facets; and (c) neighboring configurations near SP (i, j) for $i = 1-6$ and $j = 1-6$, where SP (1,1) and SP (6,6) are located at the top-left and bottom-right positions in Fig. 3.

Fig. 4(a). The reconstructed STL is regularly gridded for the even distribution of facets of identical size. Fig. 4(b) shows a group of four equal-sized facets. Three angles in a unit facet are $\pi/6$, $\pi/3$, and $\pi/2$, and for dimensionless geometrical analysis, the per unit length in the x-direction, i.e., $(\Delta x = 1)$, is set, and Δy is calculated as $\Delta y = \Delta x \tan(\pi/6) = 0.577$. The length L and width W are divided by even integers, the shortest length at angle $\pi/3$, such at $L = (2n_x)\Delta x$ and $W = (2n_y)\Delta y$, where the ratio of n_x and n_y is approximately 2. The eight facets of Fig. 4(b) have the same size as that of Facet 11. Facet 11 has axial symmetry with Facet 44 and 22 along the x- and y-axes, respectively, and rotational symmetry with Facet 31. Facet 33 can be made by translating Facet 11 to the left and bottom as much as Δx and Δy, respectively, and Facets 41, 21, and 12 can be easily constructed using Facet 33. As the flow direction is along the x-axis, the facets are well aligned in the flow direction and its orthogonal direction. These facets are only to reconstruct the STL file of high skewness, and the tetrahedron meshes will be independently generated on the basis of the reconstructed structure.

STL Reconstructing Algorithm

For CFD simulations of a flow field within a narrow space between the top surface of the bottom plates, the interplate volume to be occupied by the fluid is characterized as follows. The volume bounded by the top and bottom plates were obtained, as listed in Table 1, using admesh software, available in most Linux distributions. The four boundary surfaces of each SP are named as left $(-\hat{x})$, right $(+\hat{x})$, front $(-\hat{y})$, and back $(+\hat{y})$, where the unit vectors in the parentheses indicate outward directions normal to the surfaces. These four side-boundaries are cut perfectly vertically, as implied in Fig. 3. Specifically, the left-most and right-most boundaries of Fig. 1 and 3 have coordinates of $x_L = 343.00$ mm and $x_R = 1{,}355.00$ mm, respectively, and their difference is the length L of the HEx, i.e., 1,012 mm, as listed in Table 1. Similarly, for the front and back surfaces, the y-coordinates are set as $y_F = -185.50$ mm and $y_B = 750.50$ mm, respectively, and their difference is the width of the HEx (i.e., 936.00 mm). The length and width of the HEx were divided by $2n_x$ and $2n_y$, respectively, with a specific ratio of n_x/n_y to generate a unit facet, shown in Fig. 4. Therefore, the total $2n_x \times 2n_y$ points are made within a vertically projected plane on the x–y coordinates. The minimum and maximum points of the internal volume (for fluid) in the z-direction is observed as 6.787 and 13.29 mm, respectively, using admesh software. The fluid volume is made between $z_{\min} = 6.787$ mm and $z_{\max} = 13.29$ mm, which is above the x–y plane at $z = 0$, where the ray-tracing is initiated.

The reconstruction algorithm developed in this work is based on the standard ray-tracing algorithm, which is to convert the STL structures of Figs. 2–4. Details are as follows. The ray-tracing algorithm is, in principle, a rendering technique to generate an image by tracing the path of light in which the path of light is obtained by calculating a distance from a position of a light source to a reflecting surface of a solid object. By ejecting light rays in the whole solid angle of 4π, one can generate full 3D images, seen by the position of the light source. This method is adapted to identify the positions of the top and bottom surfaces of the interstitial fluid volume between two HEx plates, as shown in Fig. 5. As surface geometry consists of a number of connected triangles in the STL format, the top and bottom surfaces are composed of triangles of various sizes. All the facets belonging to the bottom and top plate surfaces are scanned and each facet is tested to check whether the vertical ray in Fig. 5 passes through the internal triangular zone of the facet. Using the three vertices of a facet, the equation of a (infinite) plane, including the triangle, can be calculated in a form of

$$\boldsymbol{n} \cdot (\boldsymbol{r} - \boldsymbol{p}_0) = 0 \tag{1}$$

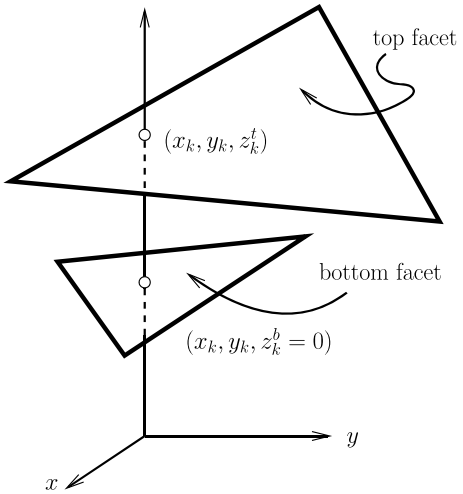

Fig. 5. Schematic of the ray-tracing algorithm to identify the z-position of the top and the bottom plates, z_k^t and $z_k^b = 0$, respectively, from the lowest position at $(x_k, y_k 0)$.

where $\boldsymbol{r}$ = position vector on a plane of a normal vector $\boldsymbol{n}$, containing a point at $\boldsymbol{p}_0$. An equation of line between two arbitrary points $\boldsymbol{r}_a$ and $\boldsymbol{r}_b$ in 3D space is

$$\boldsymbol{r} = \boldsymbol{r}_a + (\boldsymbol{r}_b - \boldsymbol{r}_a)t \tag{2}$$

where t = parameter ranging from $-\infty$ to $+\infty$. For a given position at $\boldsymbol{r}_k = (x_k, y_k, 0)$, $\boldsymbol{r}_a = \boldsymbol{r}_k$ and $\boldsymbol{r}_b = (x_k, y_k, z_{\max})$, where $z_{\max}$ is an arbitrary value larger than 13.28746 mm (of Table 1). For simplicity, $z_{\max} = 100$ mm was used, confirming that all the vertex points of the HEx reside between $z = 0$ and 100 mm. As the plane Eq. (1) is not restricted to the triangular area of three vertex points used to form the plane but covers an infinite plane, every plate facet will have an intersection point with the vertical ray. The substitution of Eq. (2) into Eq. (1) provides the intersection point of the line and the plane. As Eq. (1) is also valid by switching $\boldsymbol{n}$ by $-\boldsymbol{n}$, the intersection calculation does not depend on the sign of the normal vector. Note that a normal vector of a correct sign is already included in the STL file. Therefore, it is necessary to test if the intersection point is within the facet or not. For a facet, we propose the construction of three vertices, of which positions are denoted as $\boldsymbol{v}_1$, $\boldsymbol{v}_2$, and $\boldsymbol{v}_3$. Then, the area vector of the facet can be calculated as

$$\boldsymbol{A}_{123} = \frac{1}{2}(\boldsymbol{v}_2 - \boldsymbol{v}_1) \times (\boldsymbol{v}_3 - \boldsymbol{v}_1) \propto \pm\boldsymbol{n} \tag{3}$$

where $\boldsymbol{n}$ = normal vector of the facet; and a magnitude of $\boldsymbol{A}$ is equal to the triangular area of the facet. If the intersection point $\boldsymbol{p}$ is located within a triangular facet, then the surface area should be equal to a sum of three triangular areas that $\boldsymbol{p}$ and $\boldsymbol{v}_1$, $\boldsymbol{v}_2$, and $\boldsymbol{v}_3$ generate. Otherwise, the sum is larger than the original facet area

$$A_{p23} + A_{1p3} + A_{12p} = A_{123} \quad \text{if } \boldsymbol{p} \in S_{123} \tag{4}$$

$$> A_{123} \text{ otherwise} \tag{5}$$

where S_{123} indicates the triangular surface region made of three vertices 1, 2, and 3. At each base point $\boldsymbol{r}_k = (x_k, y_k, 0)$, two intersection points are presumed to be found. All of the 36 HEx pieces are reconstructed by applying the preceding ray-tracing algorithm, and the new structures were saved in separate STL-format files for independent meshing processes of the new piece-wise HEx files. A standard STL format to represent a triangle in 3D space is shown in Fig. 6, indicating that a facet consists of three position vectors of vertices and one (unit) normal vector. The reading of these data is straightforward using a computer program, and exchanging the sign of a normal vector will generate any structural inconsistency. Therefore, the original $\boldsymbol{n}$ stored in the STL file is used for consistency.

```
facet normal ni nj nk
    outer loop
        vertex v1x v1y v1z
        vertex v2x v2y v2z
        vertex v3x v3y v3z
    endloop
endfacet
```

Fig. 6. Data format of a STL triangle, where $\boldsymbol{n} = (n_i, n_j, n_k)$ is an outward normal vector, and $\boldsymbol{v}_1$, $\boldsymbol{v}_2$, and $\boldsymbol{v}_3$ are positions of three vertices forming the triangle.

Table 2. Pairing list of side-boundaries to apply CAMI boundary conditions

Pairing index	Neighbor boundary	Boundary of SP (i, j)
$(i+1, j)$	Back	Front
$(i, j-1)$	Right	Left
$(i-1, j)$	Front	Back
$(i, j+1)$	Left	Right

Mesh Merging Using Cyclic AMI Boundary Condition

As the matrix form of the SPs are 6 by 6, there are 36 equal-sized SPs, as shown in Fig. 3. Fig. 4(c) shows the indexes of 36 SPs, centered at (i, j). For mathematical indexing, both i and j runs from 1 to 6. The success of CFD simulations strongly depends on how the individual SPs are seamlessly merged at their side boundaries, which are denoted as back, left, front, and right, listed in the counter-clockwise direction about the center of SP (i, j). For inner SPs whose indexes are $2 \le i, j \le 5$, there are four side-boundaries. Pairs of the touching boundaries (i.e., interfaces) are listed in Table 2. Once all the internal interfaces are matched using CAMI boundary conditions, global boundary conditions are made as follows. The inlet of SP $(i = 1-6, j = 1)$ and outlet of SP $(i = 1-6, j = 6)$ are at the left-most and right-most side of the whole HEx, respectively. All other outer surfaces that enclose the entire HEx are set as a solid wall of zero velocity, which are the top and bottom surfaces and SP $(i = 1\ \&\ 6, j = 1-6)$.

Meshing Square Pieces

After all the subSTL files for the 36 SPs were prepared, each square-piece STL file was imported to NETGEN and meshed using the same set of meshing options stored in a file, ng.opt, containing the minimum and maximum mesh sizes. In addition, mesh-size grading describes how fast the mesh-size can decrease in space. The goal of this NETGEN meshing process is to generate a tetrahedron mesh for each SP and save it as a ASCII, the NETGEN neutral format. A full mesh will be prepared by merging the 36 submeshes of square pieces using utility functions included in OpenFOAM. In most cases, software graphical user interface (GUI) provides a convenient working environment to users. In our case, all the 36 SPs need to be meshed repetitively, and, therefore, a command line is used in a convenient way instead of the standard NETGEN GUI. The NETGEN file format and a specific NETGEN command using the command line in the Linux terminal instead of using GUI are explained in "Appendix I" and "Appendix II," respectively. Overall mesh quality statistics, obtained using OpenFOAM utility, checkMesh, is included in "Appendix III."

CFD Simulations

Boundary Conditions

As shown in Fig. 3, the final mesh was generated using a merging method, included in OpenFOAM. There are 16 SPs having four interfaces, which are located in the inner region of the HEx plate. The other 20 SPs are located at the plate edges. The six left-most/right-most SP boundaries form the inlet and outlet boundaries, respectively. All other patch surfaces were merged to form a connected wall. Specific boundary conditions are listed in Table 3. Pressure p is set at 0 at the outlet boundary, and its gradient is assumed to be nullified at the inlet boundary, $\nabla p = 0$. A specific value of inlet pressure will be determined as a CFD simulation

Table 3. Boundary conditions at the inlet, outlet, and wall surfaces

Boundary	Pressure	Velocity
Inlet	$\nabla p = 0$	*SurfaceNormalFixedValue*
—	—	*FlowRateInletVelocity*
Outlet	$p = 0$	*PressureInletOutetVelocity*
Wall	$\nabla p = 0$	*No-slip* $(U = 0)$

result. At the inlet boundary, flow velocity U was determined using either *SurfaceNormalFixedValue* or *FlowRateInletVelocity*. *PressureInletOutetVelocity* is applied for U at the outlet boundary, which uses various boundary conditions based on the flow direction. The $\nabla \boldsymbol{U} = 0$ is applied for outflow, and for inflow, U is calculated using the patch-face normal component of the internal-cell value. A no-slip boundary condition is used at all the solid wall surfaces, $U = 0$. A short-ranged molecular attraction is assumed between the solvent (seawater) molecules and wall surfaces, which is strong enough for the molecules to stick to a specific wall surface. The solvent fluid velocity should be equal to that of the wall velocity, as the solvent molecules do not slip on the wall surfaces. The relative velocity of the solvent molecules with respect to the wall is zero, indicating that on the boundary, the molecular velocity must be equal to the velocity of stationary walls.

Other Settings

As the current work focuses on the simulations of fluid flow under specific conditions, the temperature is set as 25°, which further determines the kinematic viscosity of water: $\nu = 1.0 \times 10^{-6}$ m^2/s, which is constant due to the incompressible character of water. As water is incompressible, and HEx plates are corrugated, the presence of turbulence cannot be ignored. So, we employed pisoFoam, one of the solvers included in OpenFOAM version 6, to the solve the transient, incompressible, and turbulent flow of Newtonian fluids using the pressure-implicit with splitting of operators (PISO) algorithm (Issa 1986; Issa et al. 1986). As the Reynolds number is small, we turned off the turbulent scheme for the following simulations (see the next section for details). ParaView version 5.4.0 was used to visualize the flow patterns and pressure profiles (Ahrens et al. 2005; Ayachit 2015).

Results and Discussion

Mesh Generation: Split-and-Merge Method

Fig. 7 shows the fully-developed tetrahedron-based 3D mesh structure used for CFD analysis of flow within the HEx. The top-left corner of Fig. 7 is identical to those of Figs. 1 and 3. Stripped lines dividing SPs show the interfaces between adjacent SPs, where the cyclic AMI boundary conditions are applied for the CFD simulations. The numbers from 11 to 33 indicate the indexes of SPs. The left side of SP11 is part of the inlet boundary, and its right side forms a CAMI boundary with the right-side of SP12. The back side of SP21 creates a CAMI boundary with the front side of SP11. Therefore, the inlet boundary surface consists of left-sides of SPs of 11, 21, ..., 61, and the outlet boundary consists of the right sides of SPs from 16, 26, ..., 66. All other boundary surfaces are set as impermeable and no-slip solid surfaces.

Flow Simulations

Table 4 includes hydrodynamic parameters (i.e., input and output conditions). The inflow rate to each HEx, 0.9 kg (or L)/s, is calculated as the total inflow rate 1,864.59 kg/s divided by the total number of HExs of 2,120. Using the density of water, 1.0×10^3 kg/m^3, the flow rate to each HEx is equivalent to 9.0×10^{-4} m^3/s. CFD simulation results are shown in Figs. 8–11 as the primary results of this study. Although comprehensive flow simulation is our ultimate research goal, the current paper focusses on the reconstruction of ill-conditioned STL files generated from the Auto CAD software. The subsequent CFD results show reasonably acceptable trends and physical implications, but the grid-independency is not fully tested.

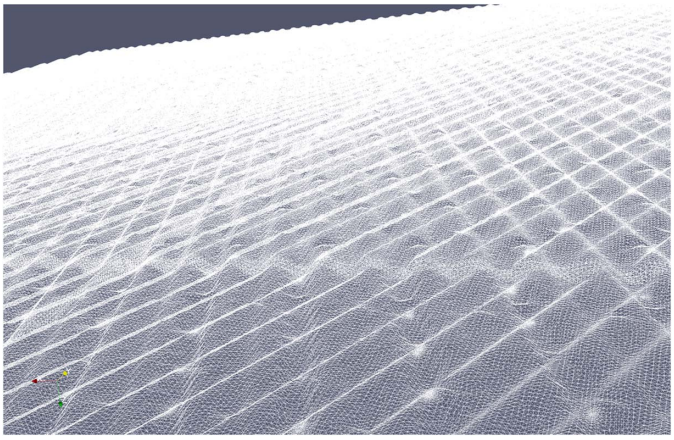

Fig. 7. Full mesh view made using the STL reconstruction. To generate this mesh using NETGEN, options for variables meshsize and min-meshsize are set as 1.0 and 0.20 mm, respectively, using the reconstructred STL file of $\Delta x = 2.0$ mm and $\Delta y = 1.154$ mm.

Table 4. Hydrodynamic parameters

Variable	Value
System inflow rate Q	1,864.59 kg/s
Total number of HExs (8 sets × 265 HEx per set)	2,120
Flow rate to each HEx	9.0×10^{-1} kg/s (9.0×10^{-4} m^3/s)

Preliminary

Fig. 8 uses only a 1/6 area of the total HEx by selecting the uppermost rectangular plate. In OpenFOAM, the pressure indicates the actual pressure divided by the fluid density: $p \rightarrow p/\rho$. The left and right portion of the rectangular plate are equal to SP11 and SP16, respectively. The CFD work shown in Fig. 8 is to test the integrity of the slit-and-mesh method, developed in this study, by visualizing standard outcomes of U and p. As this step is preliminary, specific conditions and analyses are omitted for this test run.

Low Flow Rate Case

Fig. 9 shows the flow field with the background color gradient of pressure p for the inlet flow rate of $Q = 1.466 \times 10^{-4}$ m^3/s, which is approximately 1/6 of the standard flow rate, given as 9.0×10^{-4} m^3/s in Table 1. The pressure and its gradient are set equal to zero at the (left) inlet and (right) outlet boundaries, respectively. The background color of Fig. 9 changes from red to blue indicating a gradual decrease of pressure along the flow direction of x. The pressure distribution at the inlet (of zero-gradient condition) was calculated during the CFD simulations, and its mean value is close to its maximum of 7.70×10^{-2} N · m/kg. In general, the color plot provides a clear overview of the spatial distribution of the pressure, as its gradient generates flow vectors at given position $\boldsymbol{r}$ and time t.

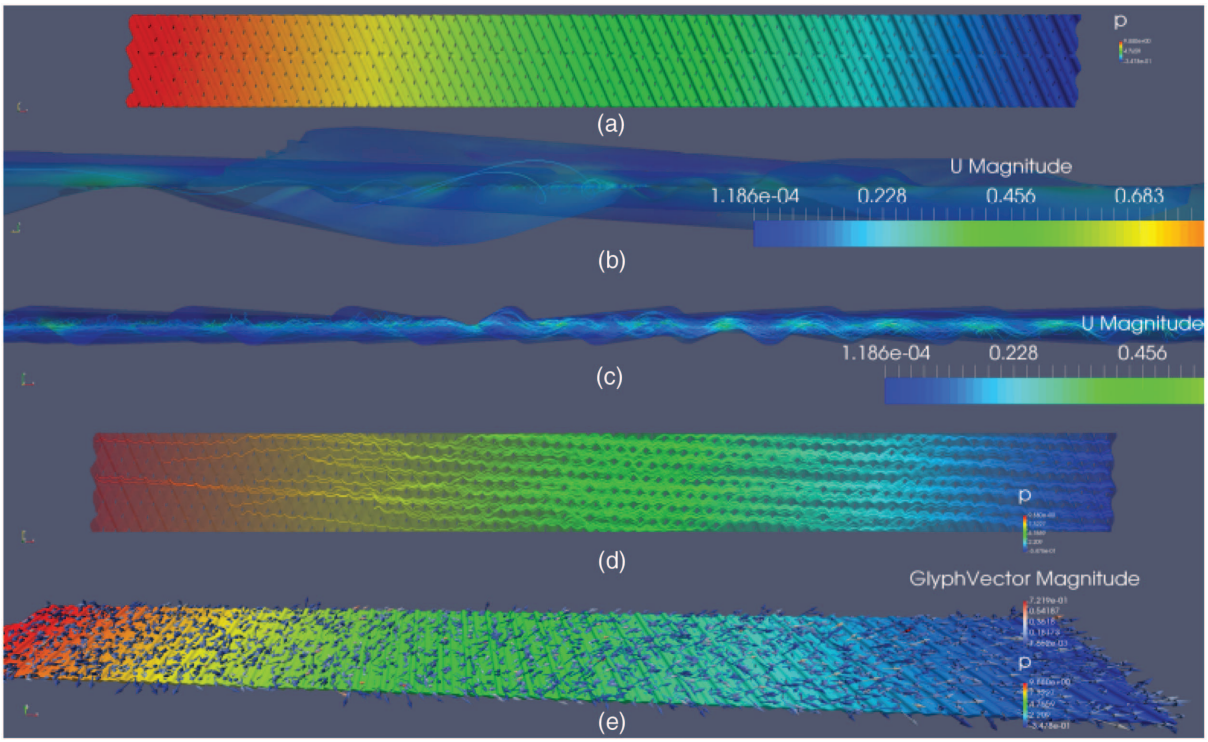

Fig. 8. (Color) Test CFD-simulation using a single rectangular plate of 1/6 size of the whole HEx, showing profiles of (a) pressure; (b and c) side views of the speed at two different viewpoints, respectively; (d) streamlines of quasi-linearity; and (e) velocity vectors with the pressure background color. (Refer to Fig. 9 for specifc values of p and $\boldsymbol{U}$.)

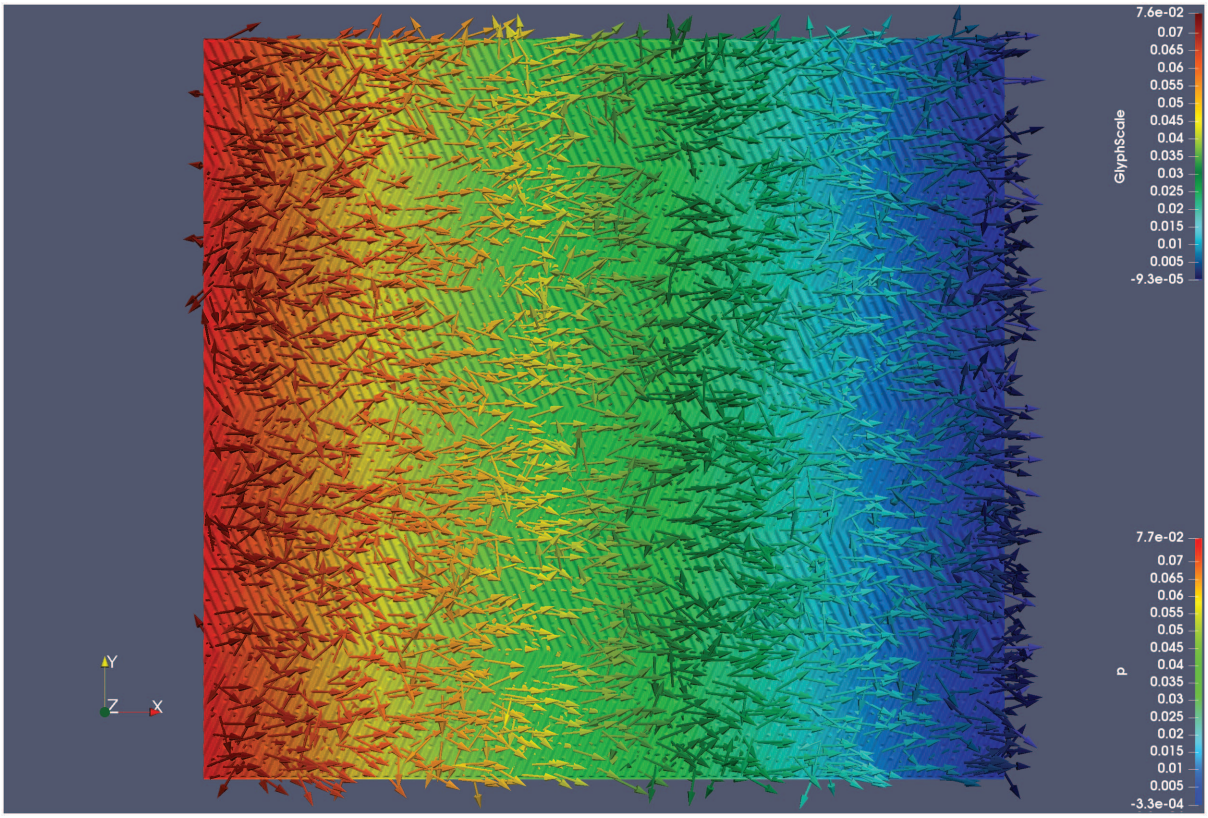

Fig. 9. (Color) Flow fields with $Q = 1.466 \times 10^{-4}$ m^3/s. The visualization scheme is equal to that of Fig. 8. The left and right sides are inlet and outlet boundaries, respectively, of which conditions are described in Table 3. All other sides are considered as impermeable walls of no flow slip.

J. Environ. Eng., 2020, 146(6): 04020040

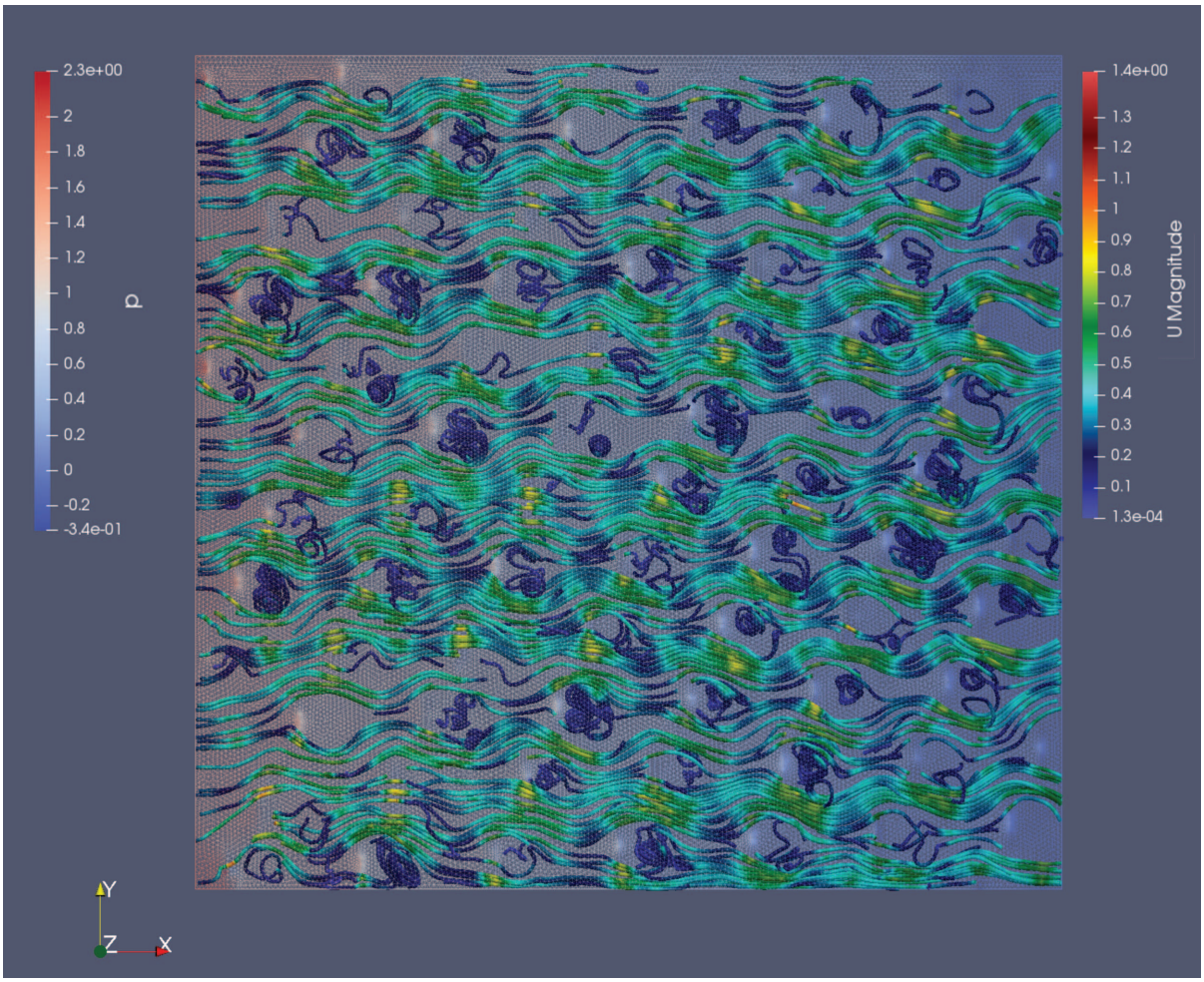

Fig. 10. (Color) Streamlines generated using the *Tube* filter function included in ParaView.

Because one of main purposes of this study is to develop a innovative meshing technique of extreme geometry, a detailed analysis of CFD results with the grid-independence are limited becasue various structures of meshes can be generated using the same STL file.

The Reynolds number (Re) regarding this HEx case can be calculated as

$$\frac{h_{\text{eq}}\langle u\rangle}{\nu} = \frac{1}{\nu}\frac{Q}{WL} \simeq \frac{O(10^{-4})}{O(10^{-6})O(1)O(1)} = O(10^{2})$$

where $\langle u\rangle = Q/h_{\text{eq}}WL$ = mean internal speed within the thin channel between two solid plates. The flow regime is primarily the laminar, and therefore, the turbulent effect may not be present even if the spatial variation of fluid flow must be complex. Fig. 10 uses the same data set of Fig. 9 and shows the streamlines of apparently sinusoidal periodic patterns. Steamlines of Fig. 10 shows vortices formed periodically along the flow direction ($+\hat{x}$), and the length scale of the periodic vortices is approximately equal to that of the horizontally long rectangular plates, packed vertically to form the whole HEx. One can visually estimate in Fig. 10 that the number of local vortices is almost equal to that of SPs (i.e., 36). As such, our future studies will include the fouling reduction method using dynamic cleaning balls within the thin flow channel. Streamlines of higher curvature indicate a longer hydraulic residence time, which must increase the heat exchanging rate. As the feed flows are composed of untreated seawater, vortex centers create a vulnerable region of surface fouling, an investigation of which will comprise our future work. The periodicity observed in Figs. 9 and 10 indicates that CFD simulation using one SP can possibly represent the effects of flow field upon the entire HEx performance. Furthermore, a basic fouling study can be conducted using only one of the SPs, shown in Fig. 3 or 7.

Fig. 11 shows the periodic intensity (magnitude) of vortices using the same original data set used for Fig. 9 and 10. A zig-zag pattern of vortex intensity is observed along the six vertically packed, long HEx plates, from the top to bottom rectangular plates. For example, the top rectangular plate shows a left-down pattern, followed by right-down and left-down of the second and third plates, respectively. The five horizontal interfaces between the long rectangular plates possess a distinct linear pattern, as the aligned vortices are merging from two adjacent plates. Lateral flows across the horizontal interfaces cause the interfacial patterns of the vortex intensity. In contrast, vertical interfaces between SPs (not apparent) in Fig. 11 do not seem to create any irregularity in the periodic vortex patterns. However, it is not clear whether the variation of vortex-intensity patterns is caused by the physical junction between two rectangular plates or the matching algorithm of the two interfacial meshes at the boundaries. The conforming degree of interfacial meshing using the CAMI algorithm influences the accuracy and stability of the numerical computation. It is expected that the vortex periodicity is closely related to the internal fouling tendencies, which will be investigated in our subsequent research.

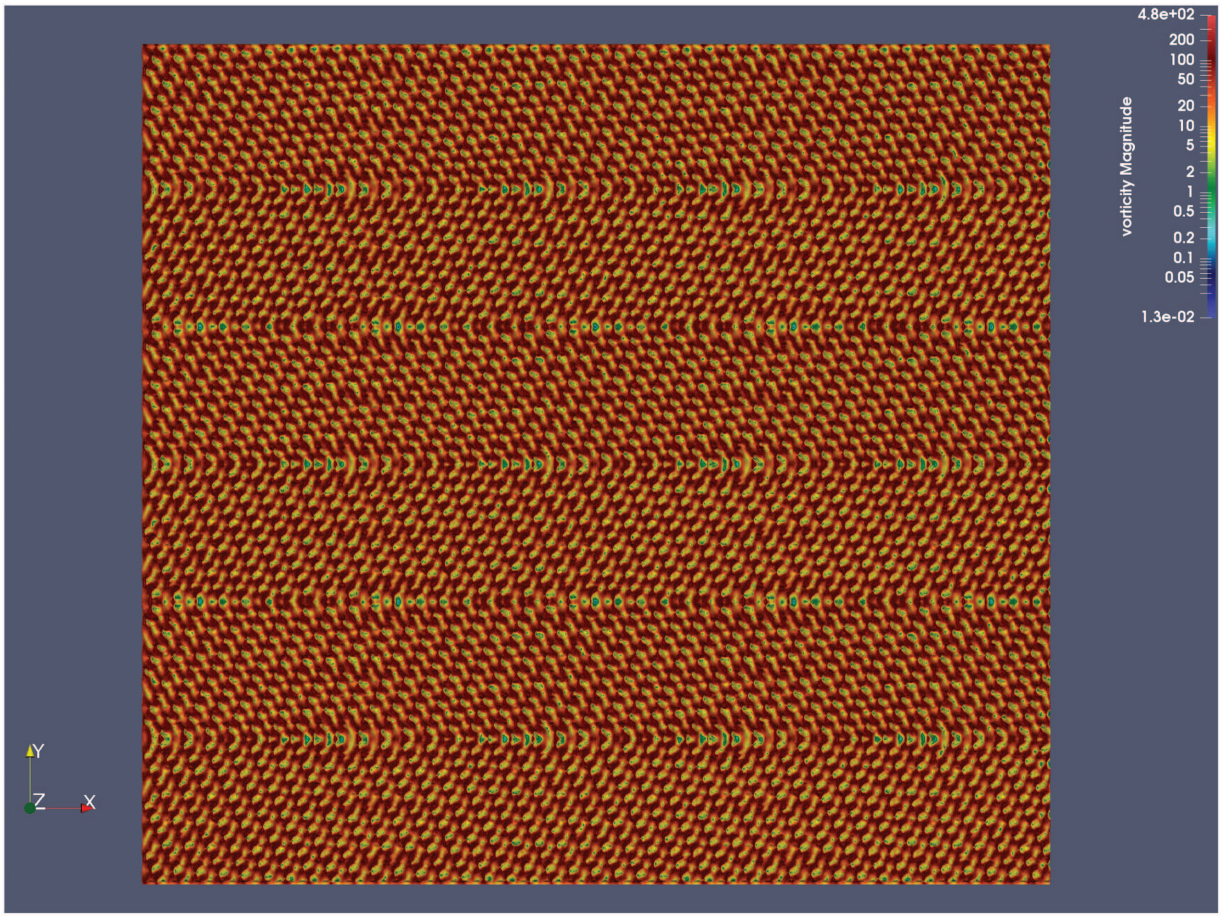

Fig. 11. (Color) Vorticity intensity visualization.

To ensure the accuracy of obtained CFD simulations, either flow field U or pressure profile p needs to be compared with experimental observations. However, the purposes of the CFD work often focus on exceptional, extreme, or unexplored cases of engineering or other types of scientific interest. In this case, self-consistent validation of the CFD work is of critical necessity. One of the standard ways for the validation of numerical CFD results exists as a grid convergence index (GCI) (ASME 2008). Specifically, the GCI and other analysis methods of numerical errors need three distinct gird sizes, $h_i(i = 1 - 3)$, and representative values of a primary variable, $\phi_i(i = 1 - 3)$, calculated at each grid size. One can calculate the grid convergence errors or iteration convergence uncertainty so as to ensure that the numerical convergence as an indirect proof of physical phenomena will occur (Ferziger and Perić 1996). However, within the recent trends of computational engineering obtaining the appropriate solution of extreme geometry or phenomena as promptly as possible has become as important as the conventional CFD work for engineering optimization in regards to the capacity limit of computational resources (Leyendecker et al. 2010). Validating numerical errors using iterative or accumulated errors is a difficult task as it confirms numerical self-consistency. In addition, a grid-size that was first implemented for CFD work is often an optimal choice for the largest, possible grid form through which numerical results can be obtained within a reasonable time duration. As our present research focuses more on the reconstruction of an ill-conditioned STL file, the CFD results allows us to propose that our algorithm is rigorous and robust enough to generate meshes that can be used for future CFD work in general.

Conforming Mesh Interfaces

Mesh Conforming Methods

When two separate objects are independently meshed and the meshes are merged by matching two boundaries to make a compound object of the two, the boundary meshes from each side must be perfectly matched for error-free data transfer from the bulk phase of one object to that of the other. If all the vertex points and edges are identically matched, then the interfacial meshes are called *conformed*. The mesh conforming requires the exchange of geometrical information of the matching boundaries and the cells located near the boundaries. Unless this information is provided prior to the meshing process, the perfect mesh conformation is challenging because the number of vertex points at the boundary of the two objects are generally different. Conceptually, there are two possible methods for mesh conforming. The first is to modify the surface mesh by relocating the vertex points of each side until perfect pairing is obtained. When the number of vertices at the boundaries are different from one side to the other, this method requires either the creation of new vertices or the destruction of preexisting vertices equal to the difference of the vertex number between two contacting sides. Although this surface-modifying method is conceptually simple and appears to be relatively straightforward, it is very challenging to create or destruct tetrahedron cell volumes containing the vertex points. Note that in most cases the tetrahedron-based meshes are generated using quality evaluation of the new vertices, and, more importantly, the secondary creation of new tetrahedron volume is based on the Delaunay triangulation (Weatherill 1992; Barber et al. 1996). The second method is to create a geometrical

contact between the two boundaries (from various objects) and exchange interpolated boundary-conditioned data obtained from one another. In general, a vertex point at one side of the contacting surface will touch an arbitrary point within a facet of the other side (OpenFoam Limited 2018). If the topologies of the boundary mesh structures are similar, the interpolation will make the large-scale CFD simulation much more feasible.

Solution Divergence

Fig. 12 shows a portion of the local AMI boundary between two SPs. The snapshot was taken when the solution diverges at a higher flow rate than $Q = 1.466 \times 10^{-4}$ m^3/s of Fig. 8, which is, at present, the maximum flow rate available for CFD simulations. To clearly visualize the numerical instabilities caused by the nonconforming interface, only six colors were used. A number of parameters were tested so as to control the numerical convergences, such as initializing the solution using a potential flow calculation, employing turbulent solvers, and increasing the number of maximum iterations with the lowest tolerable error assigned. However, the solution does not converge as the accumulated error diverges. The system sizes of investigations increase as more powerful computational resources become available at a more reasonable cost. Solution methods for large-scale problems should be more advanced than those for small systems that can be meshed, set up, and solved using small memory and serial computing schemes. As the entire geometry of the large HEx cannot be easily handled by a single CPU, the solution processes need to be modularized and parallelized. In such a situation, building optimized mesh structures that can provide the substantial stability and rapid convergence of the numerical solutions must be sought first before testing a potentially faster solving algorithm, which will be addressed within our future research. The solution divergence is due to the incomplete mesh conformation, which must be weakly related to the overall mesh quality.

Concluding Remarks

As the renewable energy production will be one of major energy generation methods, the performance of a specially designed HEx is of great importance for future OTEC. The HEx volume needed to be meshed is one of the most important preprocessing steps within flow simulations. The Auto CAD-exported steregolithography file has many highly skewed facets so that mesh-generation software often falls into an infinite loop. The original STL file was split into 36 equal-sized files of 6 by 6 array, and a STL-reconstruction algorithm was developed using the ray-tracing scheme. The mesh reconstruction was successfully conducted using the original STL file, and the newly reconstructed STL has fewer variations in sizes and types of facets because the reconstruction is grid-based on a projected plane using the ray-tracing method. Each of the subdivided STL files is meshed independently and merged into the same enclosing geometry of the original STL file. The cyclic arbitrary meshed interface (CAMI) boundary conditions are applied to seamlessly connect two adjacent parts. CFD visualizations indicate the current method, called the *split-and-merge* algorithm, provides physically reasonable computational results. The streamlines indicate that the large vortices form almost one per each SP sized $1/36$ of the whole plate. A closer investigation shows that vortices are aligned in periodic, zig-zag manners along the tangential and normal directions to the flow field, respectively. The basic flow patterns obtained in this study will be used as an input flow environment for particle hydrodynamics simulations within our future research. In addition, mesh conformation methods need to be identified so as to simulate a wide range of inlet flow rates and fully

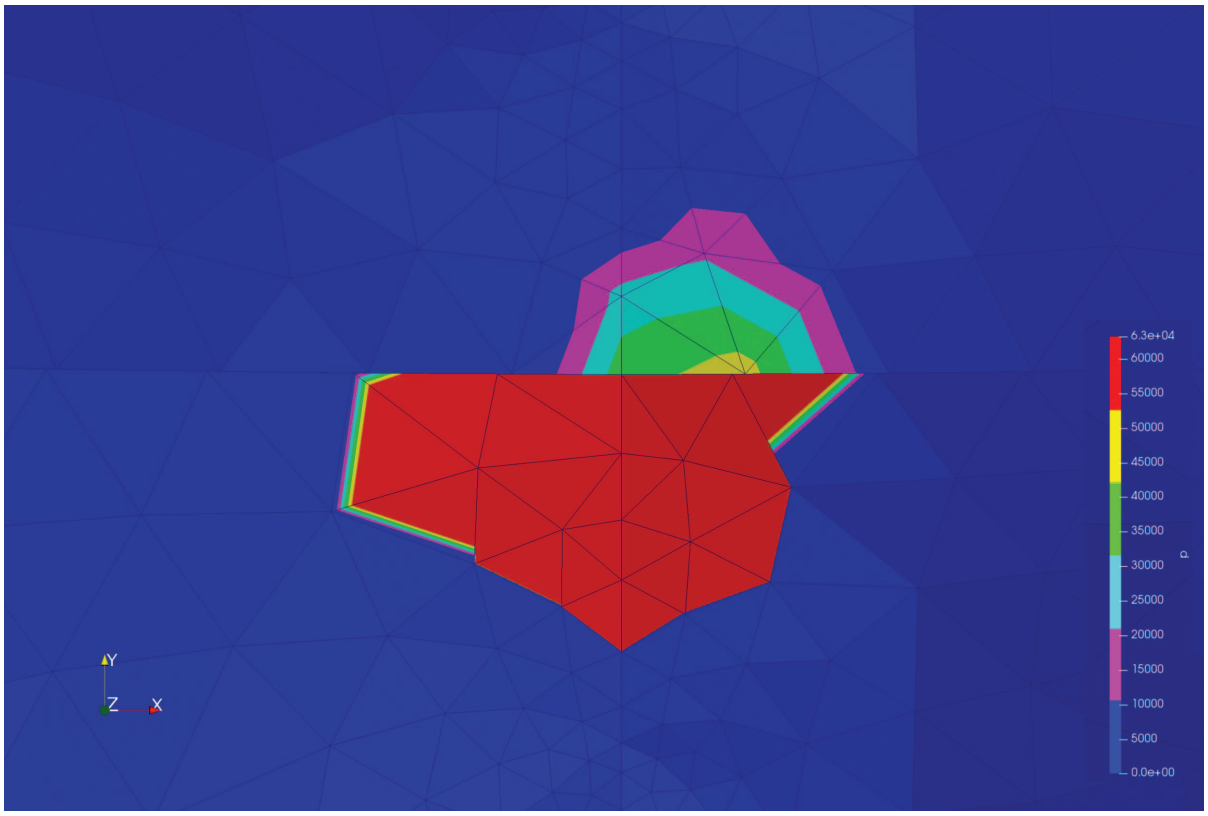

Fig. 12. (Color) Mismatching vertices on an AMI boundary with diverging p values.

J. Environ. Eng., 2020, 146(6): 04020040

optimize heat exchanging capacity and cleaning protocols of OTEC operations.

Appendix I. NETGEN Neutral

Any mesh generated by NETGEN can be exported to various formats (Schoberl 2009), such as Neutral, Surface Mesh, DIFFPACK, TecPlot, Tochnog, Abaqus, Fluent, Permas, FEAP, Elmer, STL, VRML, Gmsh, OpenFOAM (old version), JCMwave, and TET. Among them, the neutral format provides a standard and basic data structure, stored in an ASCII file. In an ASCII file of the neutral format, a tetrahedron mesh is composed of three sections: nodes, volume elements, and surface elements. Detailed contents of a neutral file is as follows:

- Line 1: N (the number of nodes (i.e., vertices);
- Line 2: x_1, y_1, z_1 (a 3D coordinate of the first node);
- ...;
- Line k: x_k, y_k, z_k (a 3D coordinate of the kth node);
- ...;
- Line $N_{\text{node}} + 1$: x_N, y_N, z_N (a 3D coordinate of the k the node);
- Line $N_{\text{node}} + 2$: N_v (the number of volume elements);
- Line $N_{\text{node}} + 3$: 1st vid, $\boldsymbol{v}_1^{(1)}$, $\boldsymbol{v}_2^{(1)}$, $\boldsymbol{v}_3^{(1)}$, $\boldsymbol{v}_4^{(1)}$;
- (The id number of the 1st volume element and indexes of four nodes composing the volume element. Unless the whole volume is compounded, the volume id value is one kind, such as 0);
- ...;
- Line $N_{\text{node}} + k$: $(k-2)$th vid, $\boldsymbol{v}_1^{(k-2)}$, $\boldsymbol{v}_2^{(k-2)}$, $\boldsymbol{v}_3^{(k-2)}$, $\boldsymbol{v}_4^{(k-2)}$;
- ...;
- Line $N + N_v + 2$: N_vth vid, $\boldsymbol{v}_1^{(k-2)}$, $\boldsymbol{v}_2^{(k-2)}$, $\boldsymbol{v}_3^{(k-2)}$, $\boldsymbol{v}_4^{(k-2)}$;
- Line $N + N_v + 3$: N_s (the number of facets);
- Line: 1st bcn, $\boldsymbol{v}_1^{(1)}$, $\boldsymbol{v}_2^{(1)}$, $\boldsymbol{v}_3^{(1)}$;
- (The boundary condition number (bcn) of the 1st facet and indexes of three nodes composing the facet. NETGEN uses 0 as the default boundary condition number);
- ...; and
- Line $N + N_v + N_s + 3$: N_sth bcn, $\boldsymbol{v}_1^{(1)}$, $\boldsymbol{v}_2^{(1)}$, $\boldsymbol{v}_3^{(1)}$.

Due to the straightforward data structure of the NETGEN neutral format, input and output functions can be developed using a standard programming language.

Appendix II. Command Line Execution for NETGEN Meshing

A specific NETGEN command is shown in Listing 1, which is to import an STL file, generate a tetrahedron mesh, and export the mesh of NETGEN neutral format. (See "Appendix I" for details of the NETGEN neutral format.)

Listing 1. NETGEN command and options. Back slashes are to break a long command.

```
1. netgen -batchmode \
2. –geofile = squarePiece11.stl \
3. –meshfile = squarePiece11.ngn \
4. –meshfiletype = "Neutral Format"
```

Appendix III. Mesh Quality Estimation Using checkMesh

The mesh quality is evaluated using OpenFOAM utility, checkMesh, piece 66 is evaluated as an example, and results are summarized as follows. Mesh statistics indicates there are 112,002 points, 910,553 faces, 744,823 internal faces, 413,844 cells, 4 faces per cell, 5 boundary patches, 0 point zones, 0 face zones, and 0 cell zones. The overall number of cells of each type are as follows: hexahedra (0), prisms (0), wedges (0), pyramids (0), tet wedges (0), tetrahedra (413844), and polyhedra (0). The following topology elements were passed: boundary definition (OK), cell to face addressing (OK), point usage (OK), upper triangular ordering (OK), face vertices (OK), and number of regions: 1 (OK). Geometry is checked as the following:

- Overall domain bounding box (1186.33 -185.333 7.28845) (1,354.67 -23.4439 13.2875);
- Mesh has 3 geometric (nonempty/wedge) directions (1 1 1);
- Mesh has 3 solution (nonempty) directions (1 1 1);
- Boundary openness (1.93818e-17 -3.72191e-17 2.4657e-15) OK;
- Max cell openness = 4.63334e-16 OK;
- Max aspect ratio = 35.125 OK;
- Minimum face area = 0.00078955. Maximum face area = 2.69351. Face area magnitudes OK;
- Min volume = 3.42138e-05. Max volume = 1.35938. Total volume = 92151.7. Cell volumes OK;
- Mesh nonorthogonality Max: 83.8359 average: 20.2337;
- *Number of severely nonorthogonal (>70 degrees) faces: 117;
- Nonorthogonality check OK;
- «Writing 117 nonorthogonal faces to set non-OrthoFaces;
- Face pyramids OK;
- Max skewness = 1.31249 OK; and
- Coupled point location match (average 0) OK.

Data Availability Statement

All data, models, and code generated or used during the study appear in the published article.

Acknowledgments

This work was financially supported by the National R&D project of "Development of 1MW OTEC demonstration plant (4/6)" (PMS4320) funded by the Ministry of Oceans and Fisheries of the Republic of Korea.

References

Abas, N., A. Kalair, and N. Khan. 2015. "Review of fossil fuels and future energy technologies." *Futures* 69 (May): 31–49. https://doi.org/10.1016/j.futures.2015.03.003.

Ahrens, J., B. Geveci, and C. Law. 2005. "ParaView: An end-user tool for large data visualization." In *Visualization handbook*. Amsterdam, Netherlands: Elsevier.

ASME. 2008. "Procedure for estimation and reporting of uncertainty due to discretization in CFD applications." *J. Fluids Eng.* 130 (7): 078001. https://doi.org/10.1115/1.2960953.

Ayachit, U. 2015. *The ParaView guide: A parallel visualization application*. Clifton Park, NY: Kitware, Inc.

Banerjee, S., M. N. Musa, and A. B. Jaafar. 2017. "Economic assessment and prospect of hydrogen generated by OTEC as future fuel." *Int. J. Hydrogen Energy.* 42 (1): 26–37. https://doi.org/10.1016/j.ijhydene.2016.11.115.

Barber, C. B., D. P. Dobkin, and H. Huhdanpaa. 1996. "The quickhull algorithm for convex hulls." *ACM Trans. Math. Software.* 22 (4): 469–483. https://doi.org/10.1145/235815.235821.

Brown, A. J. G., S. P. Neill, and M. J. Lewis. 2017. "Tidal energy extraction in three-dimensional ocean models." *Renewable Energy* 114 (Part A): 244–257. https://doi.org/10.1016/j.renene.2017.04.032.

D'Arsonal, A. 1881. "Utilization des Forces Naturelles." *La Revue scientifique.* 12 (3): 370–372.

Fang, H., H. Yao, H. Zhang, Y.-C. Huang, V. D. Hilst, and R. D. van der Hilst. 2015. "Direct inversion of surface wave dispersion for three-dimensional shallow crustal structure based on ray tracing: Methodology and application." *Geophys. J. Int.* 201 (3): 1251–1263. https://doi.org/10.1093/gji/ggv080.

Ferziger, J. H., and M. Perić. 1996. "Further discussion of numerical errors in CFD." *Int. J. Numer. Methods Fluids.* 23 (12): 1263–1274. https://doi.org/10.1002/(SICI)1097-0363(19961230)23:12<1263::AID-FLD478>3.0.CO;2-V.

Geuzaine, C., and J. F. Remacle. 2009. "Gmsh: A 3-D finite element mesh generator with built-in pre- and post-processing facilities." *Int. J. Numer. Methods Eng.* 79 (11): 1309–1331. https://doi.org/10.1002/nme.2579.

Issa, R. 1986. "Solution of the implicitly discretised fluid flow equations by operator-splitting." *J. Comput. Phys.* 62 (1): 40–65. https://doi.org/10.1016/0021-9991(86)90099-9.

Issa, R., A. Gosman, and A. Watkins. 1986. "The computation of compressible and incompressible recirculating flows by a non-iterative implicit scheme." *J. Comput. Phys.* 62 (1): 66–82. https://doi.org/10.1016/0021-9991(86)90100-2.

Levoy, M. 1990. "Efficient ray tracing of volume data." *ACM Trans. Graphics.* 9 (3): 245–261. https://doi.org/10.1145/78964.78965.

Leyendecker, S., L. J. Lucas, H. Owhadi, and M. Ortiz. 2010. "Optimal control strategies for robust certification." *J. Comput. Nonlinear Dyn.* 5 (3): 031008. https://doi.org/10.1115/1.4001375.

Mac Takahashi, M. 2000. "Ocean water and its wonderful potential." In *Deep ocean water as our next natural resource*, 9–30. Tokyo: Terra Scientific Publishing.

Marchandise, E., C. Piret, and J. F. Remacle. 2012. "CAD and mesh repair with radial basis functions." *J. Comput. Phys.* 231 (5): 2376–2387. https://doi.org/10.1016/j.jcp.2011.11.033.

Martin, A. D. 1998. "Analysis and repair of STL files." M.S. thesis, Dept. of Mechanical Engineering, California State Univ.

Nah, J.-H., H.-J. Kwon, D.-S. Kim, C.-H. Jeong, J. Park, T.-D. Han, D. Manocha, and W.-C. Park. 2014. "RayCore: A ray-tracing hardware architecture for mobile devices." *ACM Trans. Graph.* 33 (5): 1–15. https://doi.org/10.1145/2629634.

OpenFoam Limited. 2018. *OpenFOAM, the open source CFD toolbox user guide, version v1812*. London: OpenFoam Limited.

Rani, M. H., A. B. Jaafar, M. F. Yusof, A. M. Mahdzir, A. A. Awang, S. Shaukat, and H. A. A. Hassan. 2017. "Legal considerations on OTEC renewable energy deployment in Malaysia." *J. Sci. Technol. Innovation Policy* 3 (1): 34–37.

Schoberl, J. 2009. "NETGEN-4.x manual." Accessed January 24, 2009. http://netgen-mesher.sourceforge.net/docs/ng4.pdf.

Si, H. 2013. *TetGen: A quality tetrahedral mesh generator and three-dimensional Delaunay triangulator, version 1.5*. Berlin: WIAS-Software.

Si, H. 2015. "TetGen, a Delaunay-based quality tetrahedral mesh generator." *ACM Trans. Math. Softw.* 41 (2): 1–36. https://doi.org/10.1145/2629697.

Syamsuddin, M. L., A. Attamimi, A. P. Nugraha, S. Gibran, A. Q. Afifah, and N. Oriana. 2015. "OTEC potential in the Indonesian seas." *Energy Procedia* 65: 215–222. https://doi.org/10.1016/j.egypro.2015.01.028.

Ul'yanin, Y. A., V. V. Kharitonov, and D. Y. Yurshina. 2018. "Forecasting the dynamics of the depletion of conventional energy resources." *Stud. Russ. Econ. Development.* 29 (2): 153–160. https://doi.org/10.1134/S1075700718020156.

US EIA (US Energy Information Administration). 2018. "Renewable energy explained." Accessed April 15, 2019. https://www.eia.gov/energyexplained/?page=renewable_home.

Vega, L. A. 2010. "Economics of ocean thermal energy conversion (OTEC): An update." In *Proc., Offshore Technology Conf.* Reston, VA: ASCE.

Vega, L. A. 2012. "Ocean thermal energy conversion." In *Encyclopedia of sustainability science and technology*, 7296–7328. New York: Springer.

Vega, L. A., and M. Michaelis. 2010. "First generation 50 MW OTEC plantship for the production of electricity and desalinated water." In *Proc., Offshore Technology Conf., OTC 20957*, 1–17. Richardson, TX: Oshore Technology Conference. https://doi.org/10.4043/20957-MS.

Wald, I., G. P. Johnson, J. Amstutz, C. Brownlee, A. Knoll, J. Jeffers, J. Gunther, and P. Navratil. 2017. "OSPRay—A CPU ray tracing framework for scientific visualization." *IEEE Trans. Visual Comput. Graphics* 23 (1): 931–940. https://doi.org/10.1109/TVCG.2016.2599041.

Wang, T., L. Ding, C. Gu, and B. Yang. 2010. "Performance analysis and improvement for CC-OTEC system." *J. Mech. Sci. Technol.* 22 (10): 1977–1983. https://doi.org/10.1007/s12206-008-0742-9.

Weatherill, N. 1992. "Delaunay triangulation in computational fluid dynamics." *Comput. Math. Appl.* 24 (5–6): 129–150. https://doi.org/10.1016/0898-1221(92)90045-J.

Yilmaz, Y., and C. Ozturan. 2015. "Using sequential NETGEN as a component for a parallel mesh generator." *Adv. Eng. Software.* 84: 3–12. https://doi.org/10.1016/j.advengsoft.2014.12.013.

Yoon, J.-I., C.-H. Son, S.-H. Seol, H.-U. Kim, S.-J. Ha, S.-H. Jung, H.-J. Kim, and H.-S. Lee. 2015. "Performance analysis of OTEC power cycle with a liquid–vapor ejector using R32/R152a." *Heat Mass Transfer.* 51 (11): 1597–1605. https://doi.org/10.1007/s00231-015-1526-2.

Younesian, D., and M.-R. Alam. 2017. "Multi-stable mechanisms for high-efficiency and broadband ocean wave energy harvesting." *Appl. Energy.* 197 (Jul): 292–302. https://doi.org/10.1016/j.apenergy.2017.04.019.